Available online at www.sciencedirect.com
SCIENCE DIRECT®
International Journal of Heat and Mass Transfer 47 (2004) 2269–2281
International Journal of HEAT and MASS TRANSFER
www.elsevier.com/locate/ijhmt

Heat transfer from a rotating sphere interacting with a vortex

H. Niazmand, M. Renksizbulut *

Department of Mechanical Engineering, University of Waterloo, Waterloo, ON, Canada N2L 3G1

Received 13 March 2003; received in revised form 15 November 2003

Abstract

The evolution of the thermal field around a rotating/spinning sphere interacting with an advecting vortex is investigated using numerical methods in the Reynolds number range $20 \leqslant Re \leqslant 300$ for particle angular velocities of $0 \leqslant \Omega \leqslant 0.5$. It is found that particle rotation and the presence of the vortex significantly influence the heat transfer distribution locally but the time-averaged values are less affected as compared to classical laminar flow over a solid sphere. Computations in combination with surface blowing indicate that blowing significantly reduces overall heat transfer rates but has a very limited influence in damping out the transients caused by an advecting vortex. A heat transfer correlation for the vortex interaction is also provided.

1. Introduction

Heat transfer to spherical particles in uniform flow is a fundamental problem, most aspects of which are well understood and documented (e.g., [1–3]). There is however limited literature on heat transfer to small particles, such as droplets, when the flow field experiences temporal and/or spatial fluctuations. For example, in spray combustion, droplets with Reynolds numbers of the order of 10–100 [4] interact with a wide spectrum of turbulent eddies which may be viewed as a collection of vortex tubes in random walk [5].

Literature reviews on the effects of ambient turbulence on transport rates, especially in the parametric range relevant to spray combustion, indicate significant inconsistencies in the experimental observations (e.g., [6–8]). In order to identify the fundamental physics involved, an isolated vortex past a sphere in an otherwise uniform flow may be considered as a basic model, which was used by Masoudi and Sirignano [9] for the study of heat transfer to non-vaporizing droplets. They solved the Navier–Stokes and energy equations for both the gas and liquid phases numerically in the Reynolds number range of 20–100. Their results show that the time-averaged Nusselt number varies monotonically with vortex circulation strength and offset position. A heat transfer correlation containing the relevant variables was also proposed. It was also speculated that, in a spray combustion system, the vortex–droplet interactions at the Kolmogorov scale might have significant effects on the associated heat transfer rates. More recently, the same authors [10] reconsidered the problem for a vaporizing droplet and found that with surface blowing due to evaporation (Stefan flux), temporal variations in the Nusselt number due to vortex advection are usually small, suggesting that the Stefan flux effectively damps out the vortical perturbations at the droplet surface.

In spray applications, particularly when air-blast atomizers are used, droplets can acquire significant amounts of angular momentum at the time of formation, as well as in the shear layers present in the flow field. Recently, Niazmand and Renksizbulut [11] investigated the transient fluid dynamics of an isothermal interaction between a vortex tube and a rotating sphere. The associated literature has been reviewed therein, and therefore, will not be repeated here. It was shown in detail that the lift and drag coefficients are significantly influenced by the presence of the vortex. In the present work, the simultaneous effects of particle rotation, vortex interaction, and surface blowing on heat transfer to a sphere are investigated in the Reynolds number range

* Corresponding author. Tel.: +1-519-8884567; fax: +1-519-888-6197.
E-mail address: metin@uwaterloo.ca (M. Renksizbulut).

0017-9310/$ - see front matter © 2003 Elsevier Ltd. All rights reserved.
doi:10.1016/j.ijheatmasstransfer.2003.11.021

Nomenclature

a	initial vortex core radius
C_p	pressure coefficient, $(p-p_\infty)/(\rho U_\infty^2/2)$
c_p	specific heat at constant pressure
D	diameter of sphere
h	heat transfer coefficient
k	thermal conductivity
L	latent heat of vaporization
Nu	Nusselt number, hD/k
$\overline{Nu}$	time-averaged Nu
$\vec{n}$	normal unit vector
p	pressure
Pr	Prandtl number, ν/α
r, θ, φ	spherical coordinates
R	radius of sphere
Re	Reynolds number, $U_\infty D/\nu$
t	time
T	temperature, $(T_f-T_\infty)/(T_s-T_\infty)$
u, v, w	velocity components in the x, y, z directions
U_∞	free-stream velocity
$\vec{V}$	velocity vector
V_{max}	maximum tangential vortex velocity
x_c, y_c	initial vortex position

Greek symbols

α	thermal diffusivity
ε	vortex offset distance, y_c/R
Γ_0	initial vortex circulation strength, $2\pi\sigma V_{max}$
ν	kinematic viscosity
σ	vortex radius, a/R
τ	non-dimensional time, tU_∞/R
Ω	rotational speed, $R\omega/U_\infty$
ω	angular velocity

Subscripts

f	fluid
s	surface
∞	free-stream

from 20 to 300 with $Pr = 1$. A composite heat transfer correlation is also proposed, which may be incorporated to droplet models used in spray codes.

2. Problem statement and formulation

Consider a sphere of radius R and a cylindrical vortex tube parallel to the z-axis, with a core radius of σ and an initial offset distance of ε from the x-axis as shown in Fig. 1. The vortex tube is initially located 10 radii upstream from the center of the sphere and is advected with the background laminar flow in the positive x-direction. Throughout this paper, particle angular velocities around the x and z axes are referred to as *spin* and *rotation*, respectively. The vortex circulation direction is specified as counterclockwise unless otherwise stated. In order to avoid mirror image cases, particle rotation is taken clockwise in all cases.

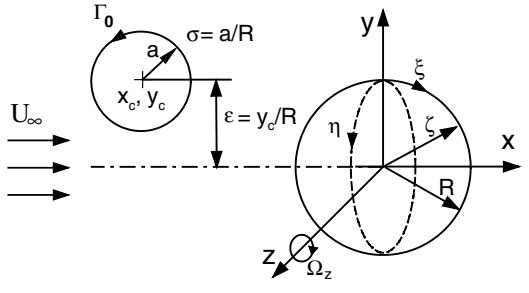

Fig. 1. Flow geometry and coordinates.

The laminar constant-property viscous flow under study is governed by the usual set of continuity, momentum and energy equations as follows:

$$\int_A \vec{V}\cdot\vec{n}\,\mathrm{d}A = 0 \tag{1}$$

$$\frac{\partial}{\partial\tau}\int_\forall \vec{V}\,\mathrm{d}\forall + \int_A \vec{V}\vec{V}\cdot\vec{n}\,\mathrm{d}A = -\int_A p\vec{n}\,\mathrm{d}A + \frac{2}{Re}\int_A \nabla\vec{V}\cdot\vec{n}\,\mathrm{d}A \tag{2}$$

$$\frac{\partial}{\partial\tau}\int_\forall T\,\mathrm{d}\forall + \int_A T\vec{V}\cdot\vec{n}\,\mathrm{d}A = \frac{2}{RePr}\int_A \vec{\nabla}T\cdot\vec{n}\,\mathrm{d}A \tag{3}$$

These equations have been non-dimensionalized using R, U_∞ and (R/U_∞) as the characteristic length, velocity and time scales, respectively. The inflow boundary conditions correspond to a uniform flow such that: $u = 1$, $v = w = 0$, $\partial p/\partial\zeta = 0$ and $T = 0$. For outflow ($\theta \geqslant 120°$), zero-gradients along the streamlines are applied to all velocity components and temperature, while pressure is set to zero. On the surface of a sphere rotating with a non-dimensional speed of $\Omega_z = R\omega_z/U_\infty$, the velocity components are

$$u = \Omega_z\cos\varphi\sin\theta, \quad v = \Omega_z\cos\varphi\cos\theta, \quad w = 0 \tag{4}$$

Similarly, the velocity components for a sphere spinning with Ω_x around the x-axis are

$$u = 0, \quad v = \Omega_x\sin\varphi\sin\theta, \quad w = \Omega_x\cos\varphi\sin\theta \tag{5}$$

The instantaneous heat transfer rate averaged over the surface is represented by the transient Nusselt number:

$$Nu(\tau) = \frac{hD}{k} = \frac{1}{A}\int_A \vec{\nabla} T \cdot \vec{n}\,\mathrm{d}A \tag{6}$$

and the time-averaged Nusselt number during the vortex/sphere interaction period $(\tau_2 - \tau_1)$ is given by:

$$\overline{Nu} = \frac{1}{(\tau_2 - \tau_1)}\int_{\tau_1}^{\tau_2} Nu(\tau)\,\mathrm{d}\tau \tag{7}$$

2.1. Vortex characteristics and initial conditions

The vortex has the same features as described by Kim et al. [12]. It contains a central core with a non-dimensional radius of $\sigma = a/R$, and its axis is oriented in the z-direction (Fig. 1). The initial velocity distribution within this core is that of solid body rotation, which reaches its maximum tangential value at $r = a$, denoted by $V_{\max}$ (normalized by the U_∞). For $r > a$, the vortex core induces a velocity field that vanishes as $r \to \infty$. This two-dimensional vortex tube (Rankin vortex [13]) is represented by the following stream function [12]:

$$\psi(x, y, z, t = 0) = -\frac{\Gamma_0}{2\pi}\ln[(x - x_c)^2 + (y - y_c)^2 + \sigma^2] \tag{8}$$

Here $\Gamma_0 = 2\pi\sigma V_{\max}$ is the initial non-dimensional vortex circulation at radius σ, which is assumed to be positive for clockwise rotation. The initial location of the vortex center in the $(x$–$y)$ plane is denoted by x_c and y_c as shown in Fig. 1. Maximum velocity at the vortex core $(V_{\max})$ represents the velocity fluctuation imposed on the uniform background flow and is taken to be less than the free-stream velocity. The vortex structure and its strength are fully characterized by $V_{\max}$ and σ at time $\tau = 0$. At later times, the advection, diffusion and distortion of the vortex are obtained as part of the flow field solution. The initial pressure field imposed by the vortex tube can be obtained from a balance of the centrifugal acceleration with the pressure gradient in the radial direction and has the following form [12]:

$$p_0(x, y, z, t = 0) = -\frac{\Gamma_0^2}{2\pi^2}\frac{1}{[(x - x_c)^2 + (y - y_c)^2 + \sigma^2]} \tag{9}$$

The initial velocity and pressure fields are determined by the superposition of the flow field induced by the vortex tube on the uniform free-stream as:

$$u_{t=0} = 1 + \frac{\partial\psi}{\partial y}, \quad v_{t=0} = -\frac{\partial\psi}{\partial x}, \quad w_{t=0} = 0, \quad p_{t=0} = p_0 \tag{10}$$

3. Solution method and accuracy

The governing equations given in Section 2 were solved numerically. A control-volume based integration technique was used in performing the discretization process in a generalized coordinate system (ξ, η, ζ), which in the present case lies along the spherical coordinates (θ, φ, r). The transient terms were discretized using a second-order accurate three-point backward scheme. A linear profile was assumed in the evaluation of diffusion fluxes at the control volume faces. For convective terms, a central differencing scheme with deferred correction was employed after linearizing using the best available estimates of velocity components from the previous iteration. The details of the numerical solution procedure and evidence of its accuracy are given elsewhere [11,14,15] and therefore, will not be repeated here.

4. Results and discussion

The velocity and thermal boundary layers are both affected by sphere rotation and the presence of a vortex in close proximity to the particle. Both effects break down the symmetry of the flow pattern around the sphere and influence the development of the wake dramatically, which leads to the formation of a transient three-dimensional flow around the particle.

Transient effects of the vortex/rotating–particle interaction are characterized by five parameters: vortex core size (σ), vortex offset position (ε), vortex maximum tangential velocity $(V_{\max})$, Reynolds number (Re), and particle rotational speed (Ω). Calculations were performed for Reynolds numbers up to 300 with non-dimensional angular velocities in the range $0 \leqslant \Omega \leqslant 0.5$. Rotation in the clockwise direction is considered as positive for both the vortex and the sphere. The maximum tangential velocity at the edge of the vortex core is taken in the range of $0.1 \leqslant V_{\max} \leqslant 0.4$, which can be interpreted as the level of velocity fluctuations imposed on the otherwise uniform background flow due to the presence of the vortical structure. This range for $V_{\max}$ is chosen in accordance with turbulence intensities encountered in spray combustion, which are typically in the range of 10–40% [4]. The vortex is initially located at $x_c = -10R$ and $y_c = \varepsilon R$ with an offset range of $-6 \leqslant \varepsilon \leqslant 6$ and a core radius range of $0.5 \leqslant \sigma \leqslant 4$.

Clearly, many possibilities for the vortex–particle interaction are conceivable based on the vortex parameters and Reynolds number, especially, when different axes of rotation are considered for the sphere. It is known that the most severe effects on the forces acting on the particle occur when the vortex interacts with a sphere rotating around an axis normal to the flow direction [11]. Furthermore, the effects of particle rotation and spin on the heat transfer rates in the absence of a vortex interaction are somewhat different. Numerical results [14] and experimental observations [16] have shown that increasing rotational speed at moderate

Reynolds numbers initially decreases the heat transfer rates, while an opposite trend appears at higher rotational speeds. On the other hand, present calculations for flow over a spinning sphere indicate a gradual increase in the Nusselt number with increasing spin.

In the following sections, first a general view of the temperature field variations due to particle rotation and the presence of the vortex is presented; then the role of the different vortex parameters on the heat transfer rates are analyzed. The primary focus will be on particle rotation around the z-axis, which is normal to the flow direction. Other possibilities for the orientation of the particle rotation axis are discussed in Section 4.6. It should be noted that the initial numerical disturbances in the flow parameters due to the sudden introduction of the vortex and the sphere into the uniform background flow dissipate rather fast and are not shown in the time-dependent figures discussed hereafter.

4.1. Thermal flow structure

A global view of the transient thermal patterns during a vortex interaction with a rotating sphere can be gained from Fig. 2(a–c), which show a sequence of the instantaneous isotherms and pressure coefficient contours for the case of $Re = 100$, $\Omega_z = 0.25$, $V_{\max} = 0.4$, $\varepsilon = 0$, $\sigma = 1$ and $\Gamma < 0$, henceforth called the *base-case*. For a particle rotating around the z-axis, symmetry is maintained with respect to the $(x$–$y)$ plane since the cylindrical vortex advects with its axis remaining parallel to the z-axis. Hence, the isotherms in Fig. 2(a) are symmetric with respect to the x-axis. The vortex is initially introduced to the flow field at the same temperature as the background flow, and therefore, does not produce thermal disturbances in the flow field. Consequently, the vortex position with respect to the particle in the thermal field is only traceable when the vortex interacts with the particle thermal boundary layer and its wake. However, the motion of a low-pressure region associated with the vortex core makes the pressure coefficient contours shown in Fig. 2(c) a suitable tool for tracing the vortex behavior.

As stated earlier, the sphere is suddenly placed in a uniform flow and at the same time the vortex is introduced $10R$ upstream of the particle. Initially the vortex advects with the superimposed uniform flow; thus at

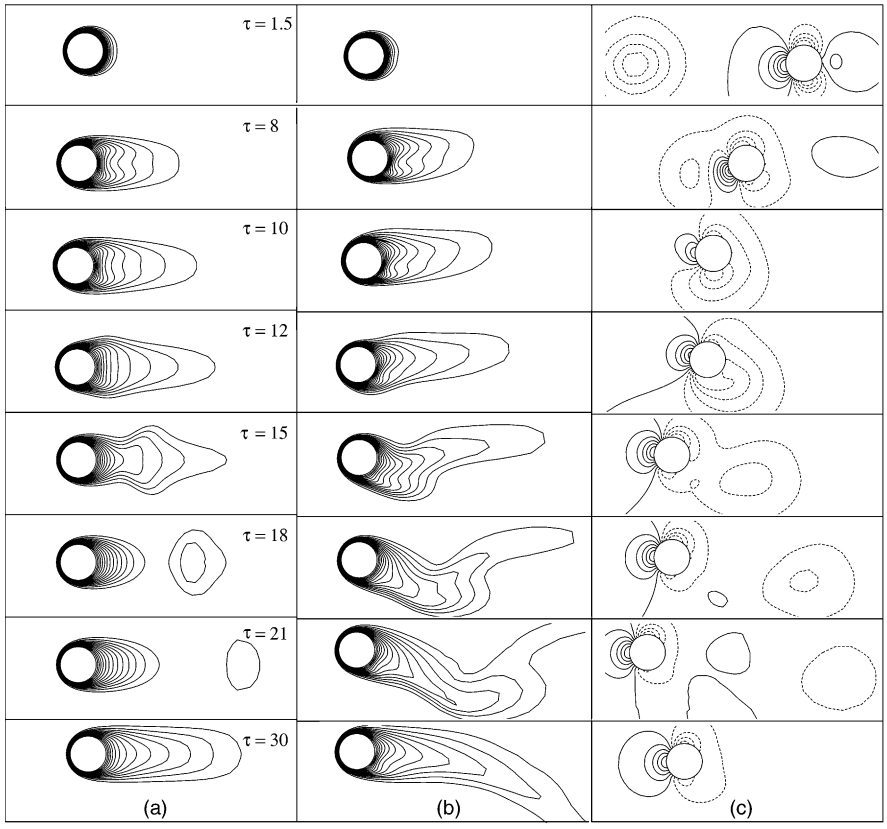

Fig. 2. Flow over a clockwise rotating sphere at $Re = 100$ and $\Omega_z = 0.25$ interacting with a counterclockwise rotating vortex at $V_{\max} = 0.4$, $\varepsilon = 0$ and $\sigma = 1$: (a) isotherms in $(x$–$z)$ plane, (b) isotherms in $(x$–$y)$ plane, both with $\Delta T = 0.07$ for $0.07 \leqslant T \leqslant 0.91$; (c) pressure contours in $(x$–$y)$ plane with $\Delta C_p = 0.178$ for $-0.7 \leqslant C_p \leqslant 0.9$ (dashed lines used for negative values).

$\tau = 1.5$, the center of the counterclockwise rotating vortex tube has moved about less than a diameter toward the particle, while a thin thermal boundary has formed around the particle. The edge of the vortex core almost reaches the front stagnation region of the sphere at about $\tau = 8$. During this time, the thermal boundary layer has developed further around the sphere and the wake has extended downstream. Particle rotation causes the $(x–y)$ plane isotherms to develop a non-symmetrical pattern with respect to the principal flow axis. Later, with its center still approaching the sphere surface, the vortex starts passing around the lower hemisphere at about $\tau = 10$. It is clear from the pressure contours in Fig. 2(c) that the center of the vortex remains below the principal flow axis as it moves downstream into the wake region. This causes the isotherms to shift towards the bottom of the particle in the $(x–y)$ plane, while in the $(x–z)$ plane the position of the vortex can be identified from the expansion of the isotherms along the axis of the vortex tube. This cross-flow expansion in the $(x–z)$ plane is discernable in Fig. 2(a) at $\tau = 12$ and becomes more clear at $\tau = 15$. At later times, $\tau \geqslant 18$, the isotherms in the $(x–y)$ plane are displaced farther towards the underneath of the particle such that a separated thermal region emerges in the $(x–z)$ plane, which disappears at later times as the vortex moves sufficiently far downstream. More details about the fluid dynamical aspect of the vortex interactions with rotating spheres can be found in Refs. [11,12].

4.2. Effects of vortex strength

The effects of vortex strength on the heat transfer coefficient are studied by varying $V_{\max}$ in the base-case identified in Section 4.1. For a vortex with a given core size, the vortex strength Γ is directly proportional to the maximum tangential core velocity $V_{\max}$. Clearly, vortices with larger $V_{\max}$ induce stronger fluctuations in the background flow and are potentially more influential on the heat transfer rates.

Fig. 3 shows the temporal variation of the Nusselt number for $V_{\max} = 0.1$, 0.2, 0.3 in addition to the base-case value of $V_{\max} = 0.4$. The Nusselt number history for classical laminar flow past a solid sphere (non-rotating sphere and no vortex interaction, henceforth called the *classical-flow*) is also included in this figure for comparison. All cases show a reduction in the Nusselt number when the vortex is in the vicinity of the particle ($\tau \approx 9$). This can be explained by the fact that a counterclockwise rotating vortex ($\Gamma < 0$) initially located on the flow axis ($\varepsilon = 0$), passes underneath the particle [11], and in the process, reduces the convective effects around the front stagnation region. After passing the particle at about $\tau = 12$, the vortex resides in the lower part of the wake and enhances convective effects in the wake region, which increases the heat transfer rates from the rear

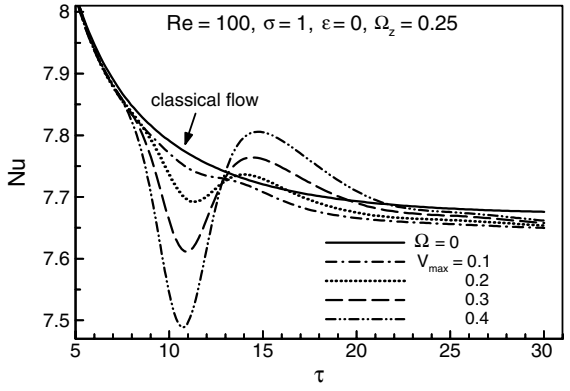

Fig. 3. Time histories of the heat transfer coefficient for different vortex strengths. Classical flow is uniform laminar flow past a non-rotating solid sphere without any vortex interaction.

hemisphere. As the vortex moves further downstream, it becomes less influential and for all vortex strengths, the Nusselt numbers approach a constant value corresponding to $\Omega_z = 0.25$, which is slightly lower than the classical-flow value.

In Fig. 4, the effects of both particle rotation and vortex circulation direction on the transient behavior of the Nusselt number are shown. For a non-rotating sphere, positive and negative Γ produce mirror image solutions; however, for a rotating particle, two independent solutions are obtained based on the vortex circulation direction. For uniform flow (no vortex present) over a clockwise rotating sphere, it is known [14] that the location of the high heat transfer region shifts to the upper hemisphere. Since, a clockwise rotating vortex ($\Gamma > 0$) also increases convective transfer in this region, an increase in the Nusselt number is observed during the approach time, $\tau \leqslant 8$. At later times, the vortex passing over the upper part of the particle leads to a decrease in the heat transfer rates because of

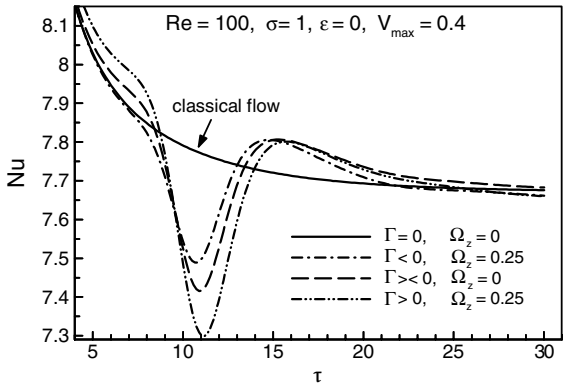

Fig. 4. Effects of vortex circulation direction.

the opposing nature of the vortex circulation direction to the flow in this region. Note that this reduction is larger than the corresponding value for a counterclockwise rotating vortex because a counterclockwise rotating vortex passes around the lower hemisphere where the region of lower heat transfer is located due to particle rotation. As expected, the transient distribution of *Nu* for a non-rotating particle lies in between the above cases, except for late times, when it approaches the case with no vortex interaction, whereas the rotating particle cases stay slightly below the cases with no vortex interaction.

It is also worth examining the surface distribution and the average values of the heat transfer rates for one of the above cases. However, a non-rotating case is considered first for reference. Fig. 5 shows the surface distribution of the Nusselt number for flow over a non-rotating sphere interacting with a counterclockwise rotating vortex at three time levels: $\tau = 7.5$ when the vortex center is located about $2.5R$ upstream, $\tau = 10$ when the vortex is

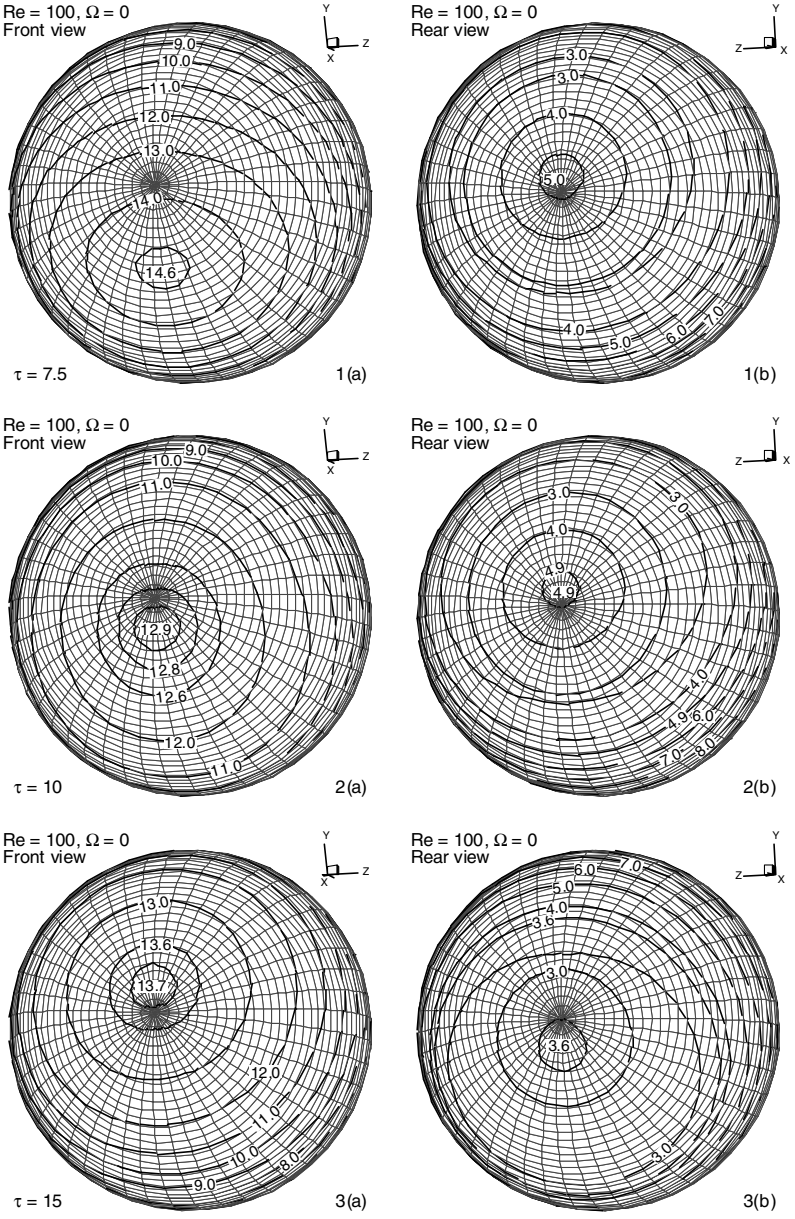

Fig. 5. Local Nusselt number distributions for $Re = 100$, $\Omega_z = 0$, $V_{max} = 0.4$, $\varepsilon = 0$ and $\sigma = 1$ at three time levels: 1(a,b) $\tau = 7.5$, 2(a,b) $\tau = 10$, 3(a,b) $\tau = 15$.

located under the sphere, and $\tau = 15$ when the vortex almost leaves the attached wake. In this figure, frame combinations (a,b) show the three-dimensional front and rear views of the *Nu* distributions. For classical flow over a solid sphere, it is well known that the maximum heat transfer region is located around the front stagnation point, and that *Nu* continuously decreases towards the separation point, beyond which an increase in the heat transfer rate is observed owing to the convective effects of the recirculating wake. In contrast, during its approach ($\tau < 10$), a counterclockwise rotating vortex causes the front stagnation point to move significantly downward [11]. As shown in Fig. 5(1a), at $\tau = 7.5$, the region of maximum heat transfer has shifted to the lower hemisphere ($\theta \cong -30°$) while the local high heat transfer region in the rear hemisphere has moved slightly upwards. During the passage of the vortex around the bottom of the sphere ($\tau > 9$), the pressure distribution in the front hemisphere undergoes an important change, which results in the gradual displacement of the stagnation region from the lower part to the upper part. At $\tau = 10$ the region of the maximum *Nu* has moved to $\theta \cong -10°$ as shown in Fig. 5(2a), while its value has decreased slightly (as explained earlier in relation to Fig. 3). Note that surface-averaged *Nu* is minimum at $\tau \approx 10$. At $\tau = 15$, the region of highest local heat transfer has moved to the upper hemisphere ($\theta \cong 10°$) and the local high *Nu* at the back has moved to the lower hemisphere. As the vortex moves farther downstream, the *Nu* distribution approaches that of the classical flow as expected.

In Fig. 6(1–3), the surface distributions of the Nusselt number for the same flow conditions as in Fig. 5(1–3) but for a rotating particle ($\Omega_z = 0.25$) are shown. Evidently, particle rotation influences the local *Nu* distribution significantly. At $\tau = 7.5$ in Fig. 6(1a), a region of high heat transfer rate in the lower front half at almost the same location as the non-rotating case is discernable. In addition, two new regions of the same Nusselt number have appeared on the upper front hemisphere, located symmetrically with the $(x$–$y)$ plane. Furthermore, the regions of lowest *Nu* are also located symmetrically on the upper hemisphere as seen in Fig. 6(1b). Both the front and rear views of the Nusselt number distributions are entirely different from the corresponding views for a non-rotating particle. More details about the fluid flow and physics behind this rather unusual thermal pattern can be found in Ref. [14]. At $\tau = 10$, similar to the non-rotating case, the region of the local high *Nu* in the lower front half has moved upward, while its value has decreased. No major changes have occurred in the rear hemisphere. Finally, at $\tau = 15$, only two regions of high *Nu* are located in the upper half, while the conditions on the rear hemisphere have changed significantly as compared to the previous time level. Now the regions of lowest heat transfer rate are located on either side of the rear stagnation point.

Despite the fact that particle rotation brings about drastic changes in the heat transfer distribution locally, the surface-averaged values of *Nu* are quite insensitive to particle rotation. Furthermore, calculations for the present case show that the time-averaged Nusselt numbers for $0.1 \leqslant V_{\max} \leqslant 0.4$ are very close to the *Nu* values of the classical flow. As shown in Fig. 3, decreases in the Nusselt number are followed by increases, and therefore, the time-averaged variation is small.

4.3. Effects of vortex size

The effects of the vortex core size on heat transfer are studied by performing computations with $V_{\max} = 0.3$ and five different core sizes: $\sigma = 0.5$, 1, 2, 3, 4. The temporal behavior of the Nusselt number is presented in Fig. 7, where two non-rotating cases are also included for comparison. This figure shows that the Nusselt number distributions for all core sizes follow a similar trend, and that increasing the vortex size to sphere diameter ratio intensifies the deviation of the *Nu* distribution from that with no vortex interaction. The fact that the Nusselt number distribution for $\sigma = 4$ essentially coincides with that for $\sigma = 3$ indicates that larger vortices will not be more influential on the heat transfer rates. For a given $V_{\max}$, the vortex strength is directly related to the vortex core size, and therefore, vortices with larger radii introduce stronger secondary flows and thus create stronger convective effects. However, with large vortices, the particle is essentially embedded inside the vortex and the local flow field around it is weakly modified by the superimposed convection associated with the vortex. Fig. 7 also shows that, for the case of $\sigma = 4$, the temporal variation of the heat transfer coefficient for a non-rotating particle approximately follows its rotating counterpart. This indicates that particle rotation does not play an important role on the transient behavior of *Nu* when the vortex size is in the range of its maximum effectiveness.

4.4. Effects of vortex offset position

To examine the effects of initial vortex offset distance from the principal flow axis, computations were performed with $V_{\max} = 0.2$ and $-6 \leqslant \varepsilon \leqslant 6$. Since positive and negative offset positions lead to different temporal behavior, they are presented separately in Fig. 8.

Fig. 8(a) shows the temporal changes in *Nu* for positive offset distances, $0 \leqslant \varepsilon \leqslant 6$ for flow over a rotating sphere ($\Omega_z = 0.25$) at $Re = 100$, interacting with a counterclockwise rotating vortex of core radius $\sigma = 1$. The *Nu* variation for flow over a non-rotating sphere in the absence of a vortex is also included for comparison. This figure indicates that the strongest *Nu* temporal variations occur when the initial vortex position is about a diameter away from the flow axis. Furthermore, there

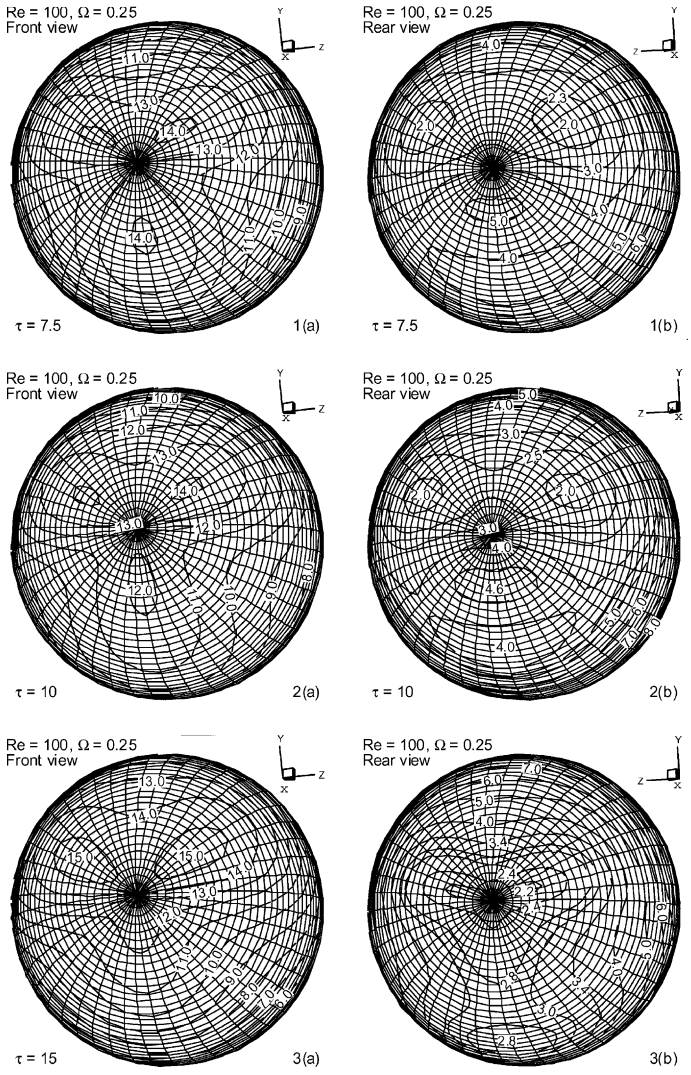

Fig. 6. Local Nusselt number distributions for $Re = 100$, $\Omega_z = 0.25$, $V_{\max} = 0.4$, $\varepsilon = 0$ and $\sigma = 1$ at three time levels: 1(a,b) $\tau = 7.5$, 2(a,b) $\tau = 10$, 3(a,b) $\tau = 15$.

is a striking difference between the cases of positive offset and $\varepsilon = 0$. This is because a vortex introduced upstream with $\varepsilon = 0$ has a head-on collision with the sphere and travels around the lower side of the particle [11,12], while for positive offset distances, the vortex naturally passes over the upper side of the particle. For a counterclockwise rotating vortex this leads to an increase in convective effects over a large portion of the front hemisphere, and thus, vortex circulation augments particle heat transfer.

Cases involving negative offset positions are shown in Fig. 8(b). Note that the initial vortex offset position during the approach time remains almost constant, and therefore at $\tau = 10$, when the vortex nearly reaches the particle, a counterclockwise rotating vortex with a negative offset reduces velocities along the stagnation streamline as compared to that of classical flow over a solid sphere. Consequently, due to the reduction in convective effects over the front hemisphere, *Nu* decreases. At later times, when the vortex moves far down stream, Nusselt numbers for all offset positions approach that of a rotating sphere at $\Omega_z = 0.25$. Again, the strongest deviation from the base flow occurs with offset positions of about a diameter from the principal flow axis.

In spite of the clear temporal sensitivity of the Nusselt number to the vortex passage (Fig. 8(a,b) when $\varepsilon \neq 0$), the deviations of the time-averaged *Nu* from that of classical-flow are small. The largest deviation observed in the present work is approximately 12%, whereas the largest deviation for a rotating sphere in the absence of a vortex interaction is less than 3% [14].

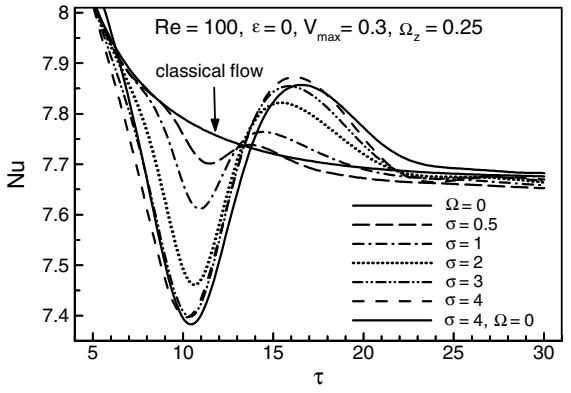

Fig. 7. Time histories of the heat transfer coefficient as a function of vortex core size.

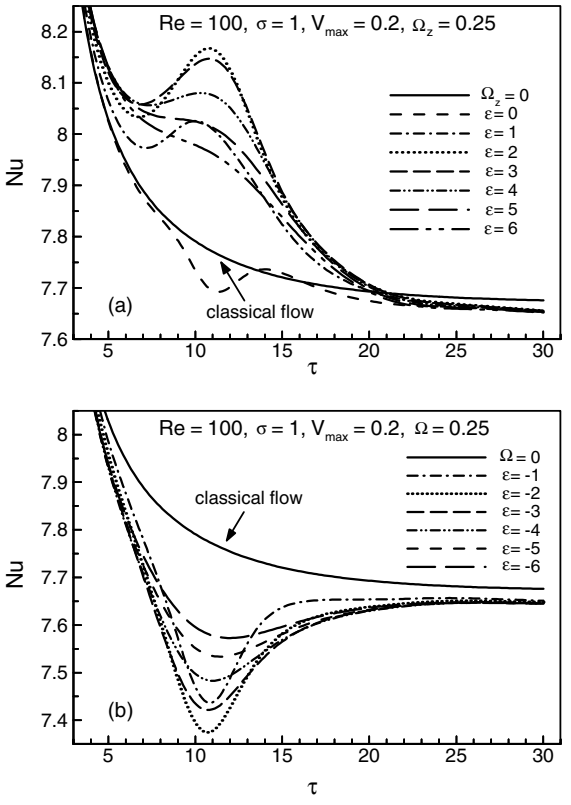

Fig. 8. Time histories of the heat transfer coefficient for different vortex offset positions: (a) positive offset, (b) negative offset.

4.5. Effects of particle rotation speed

As discussed earlier, sphere rotation significantly influences the local heat transfer distribution; however, the surface-averaged values are almost independent of particle rotation as long as $\Omega \leqslant 0.25$. Fig. 9(a) shows the transient changes in *Nu* as a function Ω_z for $V_{\max} = 0.2$, while other flow parameters remain the same as in the base-flow case. Fluid dynamics around a rotating sphere with no vortex interaction indicate that the entrainment of the flow around the particle increases with rotational speed and causes thickening of the thermal boundary layer, which in turn reduces the heat transfer rates. The case with $\Omega_z = 0.5$ shows that the heat transfer rates remain continuously below the classical-flow case.

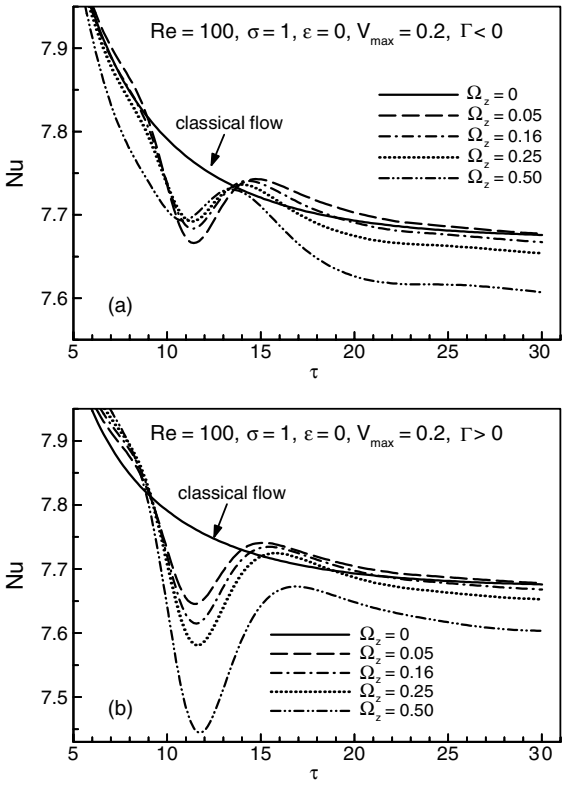

Fig. 9. Time histories of the heat transfer coefficient as a function of particle rotation speed for: (a) counterclockwise rotating vortex, (b) clockwise rotating vortex.

In Fig. 9(b), the temporal behavior of the Nusselt number for the same flow conditions but for clockwise vortex rotation is shown. A comparison of Fig. 9(a) and (b) shows that *Nu* variations show more temporal sensitivity to rotational speed for cases with positive vortex circulation. As indicated earlier, a counterclockwise rotating vortex when initially placed on the flow axis ($\varepsilon = 0$) will travel around the bottom of the rotating particle, in contrast to the clockwise rotating vortex, which passes over the topside. Different flow features over the top and bottom hemispheres of a clockwise rotating sphere during the interaction with the vortex [11] lead to these temporal heat transfer characteristics.

4.6. Effects of Reynolds numbers

To examine the effects of Reynolds numbers on the heat transfer rates, five different Reynolds numbers $Re = 20, 50, 100, 200, 300$ with $V_{max} = 0.3$ and $\Omega_z = 0.25$ are considered for a vortex core radius of $\sigma = 3$ and offset position $\varepsilon = 2$. Fig. 10 shows the results along with the *Nu* variations for the classical flow. Earlier considerations indicate that more significant vortex-induced fluctuations in the transient surface-averaged *Nu* occur for larger vortex sizes and an offset distance of about one particle diameter. Therefore, the above-chosen vortex core size and offset position can provide an estimate of the upper limit of these changes for different Reynolds numbers. Apparently, the heat transfer fluctuations induced by the vortex at a given vortex strength are stronger at higher Reynolds numbers. Since viscous effects are more dominant in low Reynolds number flows, the inertial variations induced by the vortex are relatively damped. Note that the flow at $Re = 300$ has not developed into a vortex shedding wake yet. The periodic wake patterns are established after a certain period of time depending on particle rotation and other perturbations (see [14,15] for details).

4.7. Effects of the particle rotation axis

In many spray systems, droplets acquire angular velocity because of atomizer design (e.g., air-blast nozzles). Particles can also gain rotation due to the presence of boundary layers or shear layers in different engineering applications. Prior numerical computations of the flow field around a rotating sphere indicate that the strongest dynamical effects occur when the axis of rotation is normal to the main flow direction [11]. For this reason, the emphasis of the present study has been on this type of particle rotation. Yet, almost all cases considered for particle rotation (Ω_z) have been repeated for particle spin (Ω_x), which will be discussed here. In addition, a few cases involving simultaneous particle rotation and spin have been examined.

Present calculations indicate that at low spin ($\Omega_x = 0.25$), the time variation of the heat transfer coefficients are essentially the same as the non-spinning cases, even when different vortex strengths, vortex positions and core sizes are applied. However, there are slight increases in heat transfer rates owing to particle spin, which are more pronounced at late-times. This is in contrast to rotating cases, where reductions in heat transfer rates are observed.

In Fig. 11(a), time histories of the heat transfer coefficients for four different spinning speeds are plotted for $Re = 100$, $\sigma = 1$, $V_{max} = 0.3$ and $\varepsilon = 0$. The corresponding cases without particle spin and vortex interaction are also shown for comparison. Thermal behavior typical of head-on collisions discussed earlier is

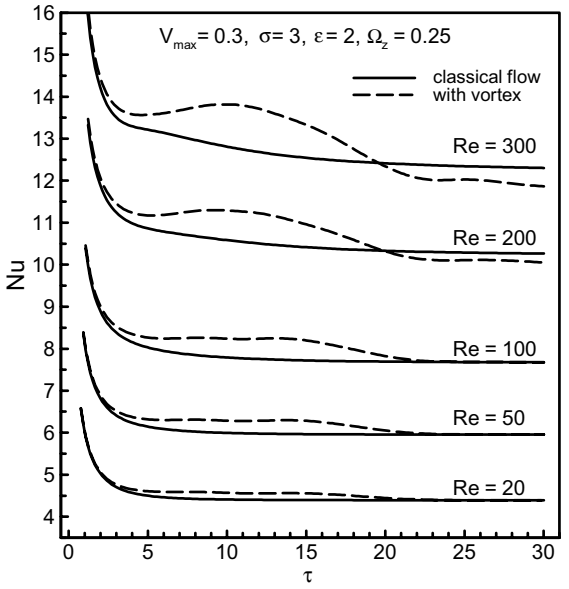

Fig. 10. Time histories of the heat transfer coefficient as a function of Reynolds number.

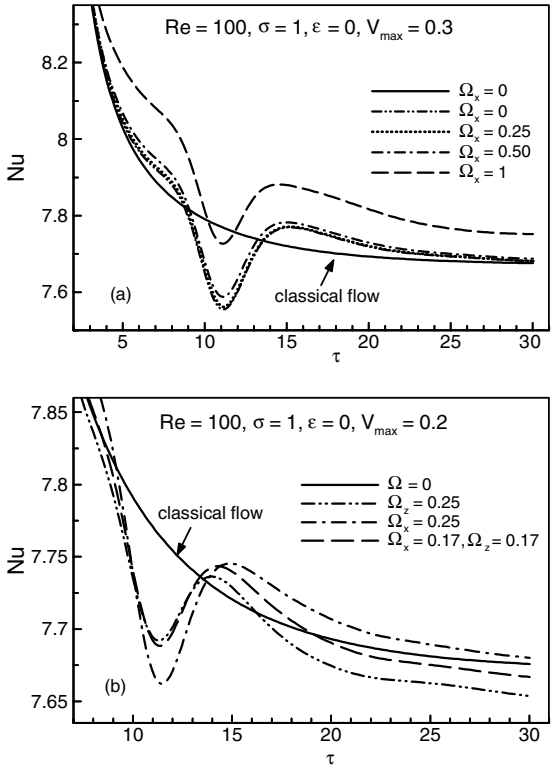

Fig. 11. Time histories of the heat transfer coefficient for: (a) different spinning speeds, (b) rotation around different axes.

observed. The positive contributions of large particle spin ($\Omega_x = 1$) shift the Nusselt number values to higher levels at all times. Furthermore, the heat transfer rates are almost insensitive to particle spin for angular velocities $\Omega_x \leqslant 0.5$.

In Fig. 11(b), the time variations of the Nusselt number for three particle rotation axes with different orientation (x-axis, z-axis, and an axis at 135° to the x-axis in the $(x$–$z)$ plane) are compared. In addition, the classical-flow results are included for comparison. The base-flow conditions with $V_{\max} = 0.2$ and $\Omega = 0.25$ for each axis are considered. At this angular velocity, Nusselt number variation is not influenced by particle spin (Fig. 11(a)); however, particle rotation reduces the heat transfer rates and also causes Nu to be more sensitive to the fluctuations caused by the vortex during the interaction time $(10 < \tau < 13)$. The case with $\Omega_x = -0.17$ and $\Omega_z = 0.17$ follows the one with particle rotation around the z-axis only, especially, during the approach and interaction times $(\tau < 13)$.

4.8. Effects of the surface blowing

In the present work, surface blowing is prescribed as $V_n = C(1 + K\cos\theta)$, where θ is measured form the front stagnation point. Coefficient C is a measure of the strength of blowing and is chosen in the range $0.01 \leqslant C \leqslant 0.04$ based on experience with droplet evaporation in high temperature flows. For non-uniform surface blowing, K is set equal to 1, resulting in much larger surface blowing from the front hemisphere.

Fig. 12 shows the simultaneous effects of surface blowing and particle rotation on the transient behavior

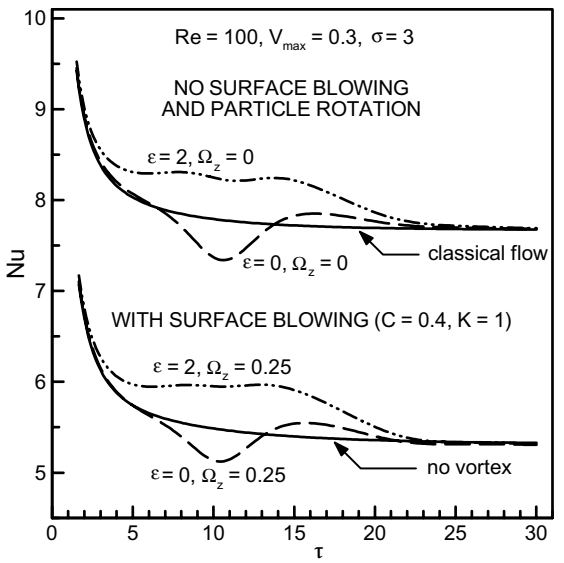

Fig. 12. Time histories of the heat transfer coefficient with and without surface blowing and particle rotation.

of Nu during the interaction of a vortex with the sphere. Non-uniform surface blowing with the strength of $C = 0.4$ is considered for $Re = 100$, $\Omega_z = 0.25$, $V_{\max} = 0.3$, and $\sigma = 3$, with two different vortex offset positions of $\varepsilon = 0$ and 2. Furthermore, classical flows over a solid sphere with and without surface blowing are included for reference. As expected, surface blowing reduces the heat transfer rates owing to the thickening of the thermal boundary layer, and therefore, a shift towards lower heat transfer rates is observed. However, the qualitative transient behavior of the heat transfer perturbations are not influenced by surface blowing as compared to the corresponding non-blowing cases. Slight changes, particularly for the case of $\varepsilon = 0$ are due to the particle rotation effects as discussed earlier with respect to Fig. 4. This is in contrast to the speculation of Masoudi and Sirignano [10] that surface blowing may damp out the vortical perturbations in heat transfer rates at the droplet surface.

4.9. A composite heat transfer correlation

Surface blowing, sphere rotation/spin, and ambient vortical structures are all expected to influence heat transfer from a sphere at varying levels. The effects of surface blowing are well established within the context of droplet vaporization and a number of reliable Nusselt number correlations exist. As for particle rotation, it is established [14] that even a low level of rotation significantly changes the heat transfer distribution locally, yet for $\Omega \leqslant 0.5$, rotation or spin has negligible affect on the time-averaged Nu as indicated earlier. Therefore, correlations developed for non-rotating vaporizing droplets are applicable to rotating spheres with a high degree of accuracy.

Heat transfer rates from a sphere can increase or decrease during a vortex encounter depending on the vortex parameters. Starting with a heat transfer correlation developed by Renksizbulut and Yuen [17] for vaporizing droplets, the following composite correlation including the effects of vortex interaction is established here:

$$Nu\left[\frac{(1+B)^{0.7}}{1-(0.03V_{\max}\varepsilon Re^{0.25})/(|\sigma-3|^{0.5}+1)}\right] = 2 + 0.57Re^{1/2}Pr^{1/3} \tag{11}$$

where $B = c_p(T_\infty - T_s)/L$ is the transfer number. Since the present study does not actually consider the vaporization of a liquid droplet, this definition of B is not applicable here. However, for prescribed surface blowing, it can be shown that $B = CRePr/Nu$, where C is the average non-dimensional blowing velocity and Nu is the computed average Nusselt number. As shown in Fig. 13, the numerical data correlated well (within ±10%) with

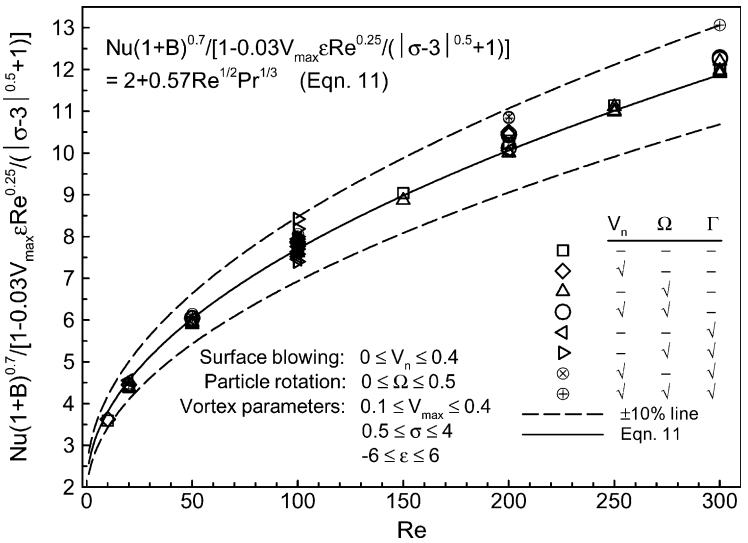

Fig. 13. A composite heat transfer correlation for flow over a rotating sphere with surface blowing and vortex interaction.

this equation. It should be noted that V_{max} is positive for clockwise vortex circulation and vice versa. Similarly, ε can be positive, negative or zero. Data originating from cases with rotation, surface blowing and their simultaneous application are taken from [14].

5. Conclusions

Transient thermal interactions between isolated vortices and rotating/spinning spheres have been studied using numerical methods. The effects of vortex features, particle angular velocity and axis of rotation, as well as simultaneous surface blowing on heat transfer have been analyzed. It is observed that the presence of the vortex and particle rotation significantly influence the heat transfer distributions locally, and to some extent, the surface-averaged transient behavior, while the time-averaged values of the Nusselt number are less affected as compared to the classical case of uniform laminar flow over a solid sphere.

It is observed that increasing in the vortex circulation strength at fixed core size results in increasingly larger deviations in the thermal behavior from that of classical-flow, whereas increasing the vortex circulation strength by increasing the vortex size at a constant V_{max} leads to a different behavior in the Nusselt number temporal behavior. Strongest deviation from base flow occurs at a certain vortex size ($\sigma \approx 3$). Obviously, for the case of very large vortices, the local flow field around the embedded sphere is very weakly modified by the advecting vortex. Similarly, a vortex passing at a far distance hardly influences the near particle flow pattern. Present calculations show that *Nu* deviations from base flow start to level out for vortices passing more than two diameters away from the principal flow axis, while the strongest temporal variations occur for the offset distance of about one diameter ($\varepsilon = \pm 2$). It is also found that with simultaneous surface blowing, the temporal variations in Nusselt number due to the advecting vortex are qualitatively similar to those when surface blowing is absent, although there is a reduction in the heat transfer rates because of the thickening of the thermal boundary layer.

The aforementioned effects appear to be stronger at higher Reynolds numbers, since viscous effects that are more dominant at low Reynolds numbers dampen the inertial fluctuations caused by the advecting vortex. It is also interesting to note that similar dependences on the vortex parameters have been observed for the drag coefficient variations [11].

Acknowledgements

The financial support of the Natural Sciences and Engineering Research Council of Canada is gratefully acknowledged.

References

[1] R. Clift, J.R. Grace, M.E. Weber, Bubbles, Drops and Particles, Academic Press, New York, 1970.
[2] S.S. Sadhal, P.S. Ayyaswamy, J.N. Chung, Transport Phenomena with Drops and Bubbles, Springer-Verlag, New York, 1997.
[3] W.A. Sirignano, Fluid Dynamics and Transport of Droplets and Sprays, Cambridge University Press, Cambridge, 1999.

[4] G.M. Faeth, Mixing, transport and combustion in sprays, Progress Energy Combust. Sci. 13 (1987) 293–345.
[5] A.J. Chorin, Vorticity and Turbulence, Springer-Verlag, Berlin, 1994.
[6] W.D. Warnica, M. Renksizbulut, A.B. Strong, Drag coefficients of spherical liquid droplets. Part2: turbulent gaseous fields, Exp. Fluids 18 (1995) 265–276.
[7] P.R. Yearling, R.D. Gould, Convective heat and mass transfer from single evaporating water,methanol and ethanol droplets, ASME Heat Transfer Fluids Eng. Div. HTD-Vol. 321/FED- Vol. 233 (1995) 33–38.
[8] I. Gokalp, C. Chauveau, O. Simon, X. Chesneau, Mass transfer from liquid fuel droplets in turbulent flow, Combust. Flame 89 (1992) 286–298.
[9] M. Masoudi, W.A. Sirignano, The influence of an advecting vortex on the heat transfer to a droplet, Int. J. Heat Mass Transfer 40 (15) (1997) 3663–3673.
[10] M. Masoudi, W.A. Sirignano, Collision of a vortex with a vaporizing droplet, Int. J. Multiphase Flow 26 (2000) 1925–1949.
[11] H. Niazmand, M. Renksizbulut, Viscous interaction between a vortex tube and a rotating spherical particle, Part. Part. Syst. Characterizat. 20 (2003) 47–61.
[12] I. Kim, S. Elghobashi, W.A. Sirignano, Unsteady flow interaction between an advected cylindrical vortex tube and a spherical particle, J. Fluid Mech. 288 (1995) 123–155.
[13] P.G. Saffman, Vortex Dynamics, Cambridge University Press, Cambridge, 1992.
[14] H. Niazmand, M. Renksizbulut, Transient three-dimensional heat transfer from rotating spheres with surface blowing, Chem. Eng. Sci. 58 (2003) 3535–3554.
[15] H. Niazmand, M. Renksizbulut, Surface effects on transient three-dimensional flows around rotating spheres at moderate Reynolds numbers, Comput. Fluids 32 (2003) 1405–1433.
[16] M.P. Noordsji, J.W. Rotte, Mass transfer coefficient for a simultaneously rotating and translating sphere, Chem. Eng. Sci. 23 (1968) 657–660.
[17] M. Renksizbulut, M.C. Yuen, Experimental study of droplet evaporation in a high-temperature air stream, J. Heat Transfer 105 (1983) 384–388.